Supplementary Material

S1| Reverse current mechanism and the origin of carbon corrosion AST protocol:

If startup/shutdown (SUSD) is performed in an uncontrolled way, i.e., when the cell is in open-circuit condition and H_2 is injected in/ejected out the anode compartment without N_2 flushing, a mixed gas front is formed between H_2 and O_2 (from air). This mixed gas front triggers a chain of electrochemical reactions inside the cell that eventually leads to carbon corrosion. The complete mechanism has been explained by Reiser et al. using a reverse-current mechanism[1]. A schematic of the corresponding electrochemical reactions (redrawn based on schematic in the reference) due to reverse current mechanism with resulting potential distribution is shown in Figure S1a.

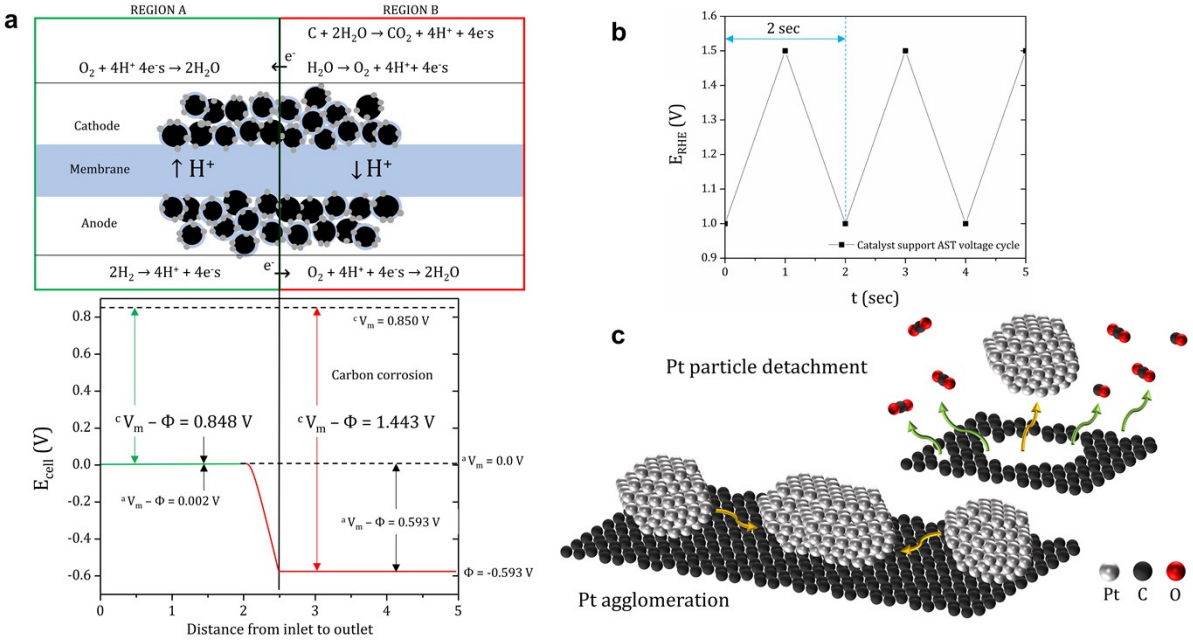

Figure S1| Fundamentals of carbon corrosion. a, Electrochemical reactions occurring inside the cell due to a mixed H_2/O_2 front at the anode with corresponding potentials in different regions of the cell. b, The DOE carbon corrosion AST voltage profile to simulate the reverse current mechanism. c, Expected catalyst degradation mechanisms- Pt detachment from carbon support and Pt agglomeration.

The DOE carbon corrosion AST voltage cycle to mimic the operation, and the major degradation modes of carbon corrosion is shown in Figure S1b. The AST was formulated to mimic the potential at cathode region B during the reverse-current mechanism. Brightman and Hinds found that the local potential in cathode region B, where carbon corrosion occurs, is approximately 1.4 V.[2] So, the AST is done by cycling the cell voltage uniformly with time in a triangular waveform with 1 V as the lower limit and 1.5 V as the upper limit. The time period is 2 seconds. As water, not gaseous O_2, oxidizes carbon (Eqn. (1)), the AST is done with H_2 at anode and N_2 at cathode in 100% RH. The voltage wave is shown schematically in Figure S1c.

Figure S1c shows the two expected catalyst degradation modes during carbon corrosion- Pt detachment from the carbon support and Pt agglomeration. It is important to note that the carbon corrosion AST is much harsher than the actual SUSD. This is because carbon only corrodes from region B of the cathode during SUSD while carbon corrodes from the entire cathode during DOE carbon corrosion AST.

S2| Electrochemical characterization protocols:

The details and the order of electrochemical experiments performed throughout the study are given in Table S1.

Table S1| Electrochemical characterization and AST protocols.

	T_{cell} (° C)	Anode					Cathode					Protocol
		Gas (-)	Flowrate (slpm)	Dew point (° C)	% RH (-)	Pressure (a) (kPa)	Gas (-)	Flowrate (slpm)	Dew point (° C)	% RH (-)	Pressure (a) (kPa)	
Voltage break-in	80	H_2	0.2	80	100	100	Air	0.4	80	100	100	0.8 V, 0.6 V and 0.3 V holds for 30 s each (~200 cycles).
Characterization												
Voltage recovery	40	H_2	0.25	48	150	150	Air	0.15	48	150	150	0.2 V hold for 1 hour.
Polarization curve	80	H_2	1	80	100	150	Air	2.5	80	100	150	4 min holds from high to low current density.
Mass Activity	80	H_2	1	80	100	150	O_2	2.5	80	100	150	3 min holds from 0.75 V to OCP with 25 mV step size.
CV, LSV and N_2 EIS	80	H_2	1	80	100	100	N_2	1	80	100	100	Scan rate of 100 $mV.s^{-1}$ from 0.1 V to 1.2 V for CV, scan rate of 1 $mV.s^{-1}$ from 0.05 V to 0.8 V for LSV and frequency sweep from 20 kHz to 0.1 Hz at 0.2 V (6 $points.dec^{-1}$) for EIS.
O_2 mass transport resistance	80	H_2	1	74.13	75	100, 150, 200 and 250	x% O_2 in N_2	5	74.13	75	100, 150, 200 and 250	3 min holds from 0.3 V to 0.06V with step size of 60 mV in 1 %, 2 % and 4 % O_2 in N_2 at each pressure.
Accelerated Stress Test												
Carbon corrosion	80	H_2	0.2	80	100	100	N_2	0.2	80	100	100	500 $mV.s^{-1}$ scan rate from 1.0 V to 1.5 V (2,000 cycles)

After 100, 500 and 2000 AST cycles

S3| NDIR data and quantification of carbon loss:

During carbon corrosion AST (1-1.5 V voltage cycling), the anode feed was 100% humidified H_2 and the cathode feed was 100% humidified N_2 at 80 C (353 K). The flow rate was 0.2 slpm for both anode and cathode. Flow pressure was 1 atm absolute. It was assumed that the inlet and outlet flow rate at the cathode were same. However, the number flow rate was different, and can be calculated as follows:

$$\frac{dN}{dt}|_{in} = \frac{dN_{N_2}}{dt}|_{in} + \frac{dN_{vapor}}{dt}|_{in} \#(S1)$$

$$\frac{dN}{dt}|_{out} = \frac{dN_{N_2}}{dt}|_{in} + \frac{dN_{vapor}}{dt}|_{out} + \frac{dN_{CO_2}}{dt}|_{out} + \frac{dN_{CO}}{dt}|_{out} \#(S2)$$

In the equations S1 and S2, it was implicitly assumed that dN_{N2}/dt is same at both inlet and outlet as N_2 does not react. $\frac{dN_{vapor}}{dt}|_{out} < \frac{dN_{vapor}}{dt}|_{in}$ as water vapor reacts with C to form CO and CO_2. The experimental data shows that CO_2 is produced at a much larger amount than CO. This happens because the potential applied, 1-1.5 V is higher than the known CO oxidation potential. So, the produced CO gets oxidized to

CO_2. The NDIR sensor measures ppm level of CO_2 and CO. The CO_2 and CO ppm readings can be converted to the C mass lost. First, the mass of CO_2 produced from the measured ppm data is estimated as:

$$m_{CO_2}(cycle) = \int_{AST\ start\ time}^{time\ when\ CO_2\ returns\ to\ base\ level} \frac{dV}{dt} n_{tot}\left(ppm_{CO_2} - ppm_{CO_2,baseline}\right) M_{CO_2} dt \#(S3)$$

$$m_{CO}(cycle) = \int_{AST\ start\ time}^{time\ when\ CO\ returns\ to\ base\ level} \frac{dV}{dt} n_{tot}\left(ppm_{CO} - ppm_{CO,baseline}\right) M_{CO} dt \#(S4)$$

In Eqn. S3 and S4, dV/dt is the volume flow rate (0.2 slpm). The net molar density of outgoing species n_{tot} is given by $n_{tot} = n_{N_2} + n_{vapor} + n_{CO_2} + n_{CO}$. Among all the quantities, n_{CO} is the most negligible one. The baseline ppm level of CO_2 and CO was subtracted because before AST, i.e., before any significant production of CO_2 or CO due to AST, the baseline ppm levels were not 0. So, that part had to be subtracted from the observed ppm level to estimate the correct ppm of CO_2 and CO that was produced due to the AST. Another important aspect of equations S3 and S4 is the upper limit of the integration. It was observed that the ppm levels return to the baseline after sometime once the AST stops, as discussed in the main manuscript. The fuel cell operation was kept in idle mode until the ppm levels returned to the baseline values. The integration was carried out until that time.

The back pressure was kept at 1 atm during the time. Here $P_{back} = P_{gas} + P_{vapor}$. P_{vapor} = saturated vapor pressure at 80 C = 47.343 kPa, which is about half of the back pressure (1 atm = 100 kPa). So, the contribution of water vapor at this high RH cannot be neglected at all. In the expression of total molar density $n_{N_2} + n_{CO_2} + n_{CO} = n_{ideal}$ where the N_2, CO, and CO_2 can be assumed to be ideal gases, and can be estimated as $n_{ideal} = \frac{P_{ideal}}{RT} = \frac{P_{back} - P_{vapor}}{RT} = \frac{P_{back} - P_{sat}}{RT}$ = 18.4 mol/m^3. Density of saturated water vapor is 293.8 gm/m^3, and the molar density of saturated vapor at 80 C = 293.8 gm/m^3 / 18.02 g/mol = 16.3 mol/m^3. So, the molar density of water vapor is almost similar to that of ideal gas. This is also expected as the vapor pressure was almost half of the back pressure. So, the saturated vapor pressure was almost equal to the pressure exerted by the ideal gas inside the NDIR chamber.

With these calculations, equations S3 and S4 can be simplified to (in units of µg):

$$m_{CO_2}(cycle) = \int_{AST\ start\ time}^{time\ when\ CO_2\ returns\ to\ base\ level} 0.0051\left(ppm_{CO_2} - ppm_{CO_2,baseline}\right) dt\ \#(S5)$$

$$m_{CO}(cycle) = \int_{AST\ start\ time}^{time\ when\ CO\ returns\ to\ base\ level} 0.00324\left(ppm_{CO} - ppm_{CO,baseline}\right) dt\ \#(S6)$$

From the mass of CO_2 and CO, mass of C lost can be calculated as:

$$m_{C_{lost}}(cycle) = \frac{3}{11} m_{CO_2}(cycle) + \frac{3}{7} m_{CO}(cycle) \ \#(S7)$$

The results of Equation S7 are plotted in main manuscript Figure 1b. Below in Figure S3, plotted are the ppm levels of CO_2 and CO (without the baseline corrections) as observed during the AST. Figure S3a to c show the CO_2 ppm levels whereas Figure S3d to f show CO ppm levels. As described in the main manuscript, the MEA II was aged for 500 cycles and MEA III was aged for 2000 cycles. So, the ppm data (for both CO and CO_2) for the first 500 cycles were averaged between these two MEAs. The ppm data for the next 1500 cycles is only from MEA III. As can be seen in Figure S3, the CO ppm levels are much lower than the corresponding CO_2 levels. This is consistent as the potentials applied (1-1.5 V) are higher than the CO oxidation potential, as a result of which, most of the CO had been oxidized to CO_2. Another feature of Figure S3 is that the CO_2 peaks are more transient than CO peaks. From Figure 1b in the main manuscript, C corrosion gets lower with ageing. CO_2 production in the first 100 cycles was approximately 168 $\mu g.cm^{-2}$, 84 $\mu g.cm^{-2}$ in the next 400 cycles, and 53 $\mu g.cm^{-2}$ in the next 1500 cycles. CO production was 26 $\mu g.cm^{-2}$ in the first 100 cycles, 71 $\mu g.cm^{-2}$ for the next 400 cycles, and 41 $\mu g.cm^{-2}$ in the next 1500 cycles. As seen from the data, the rate of carbon corrosion decreases with ageing. It might be because carbon oxidation takes place mostly in the amorphous part, while the crystalline graphitic part does not corrode as much. This result has been found in many studies, as mentioned in the introduction section of the main manuscript.

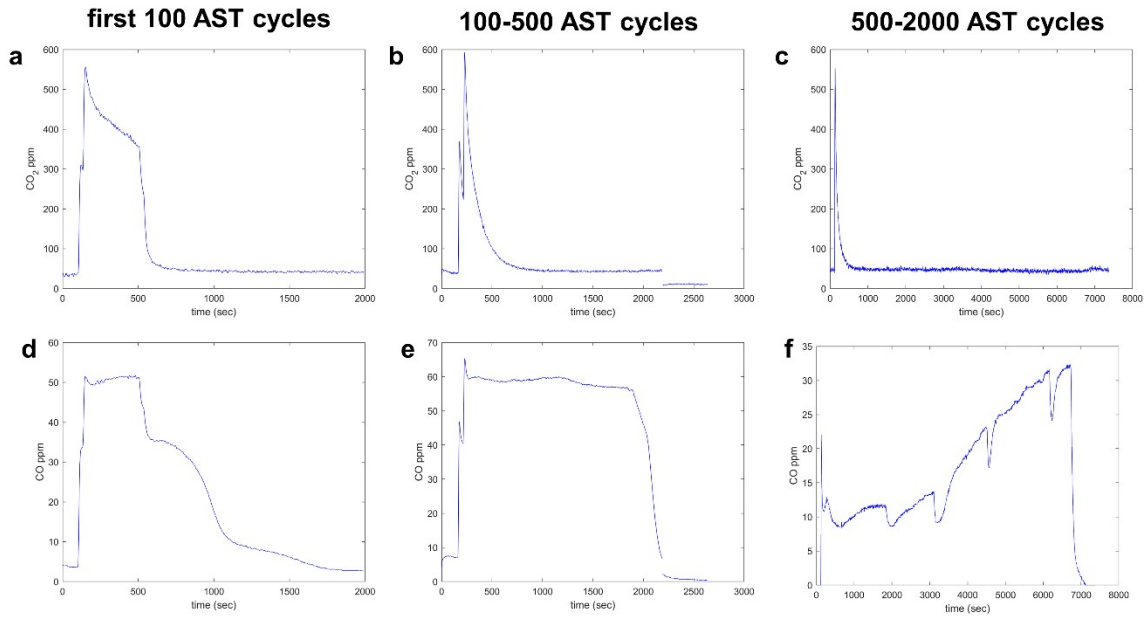

Figure S2| Non-dispersive infrared (NDIR) sensor data (in ppm) of CO_2 and CO during the AST voltage cycling.

S4| SEM thickness measurement:

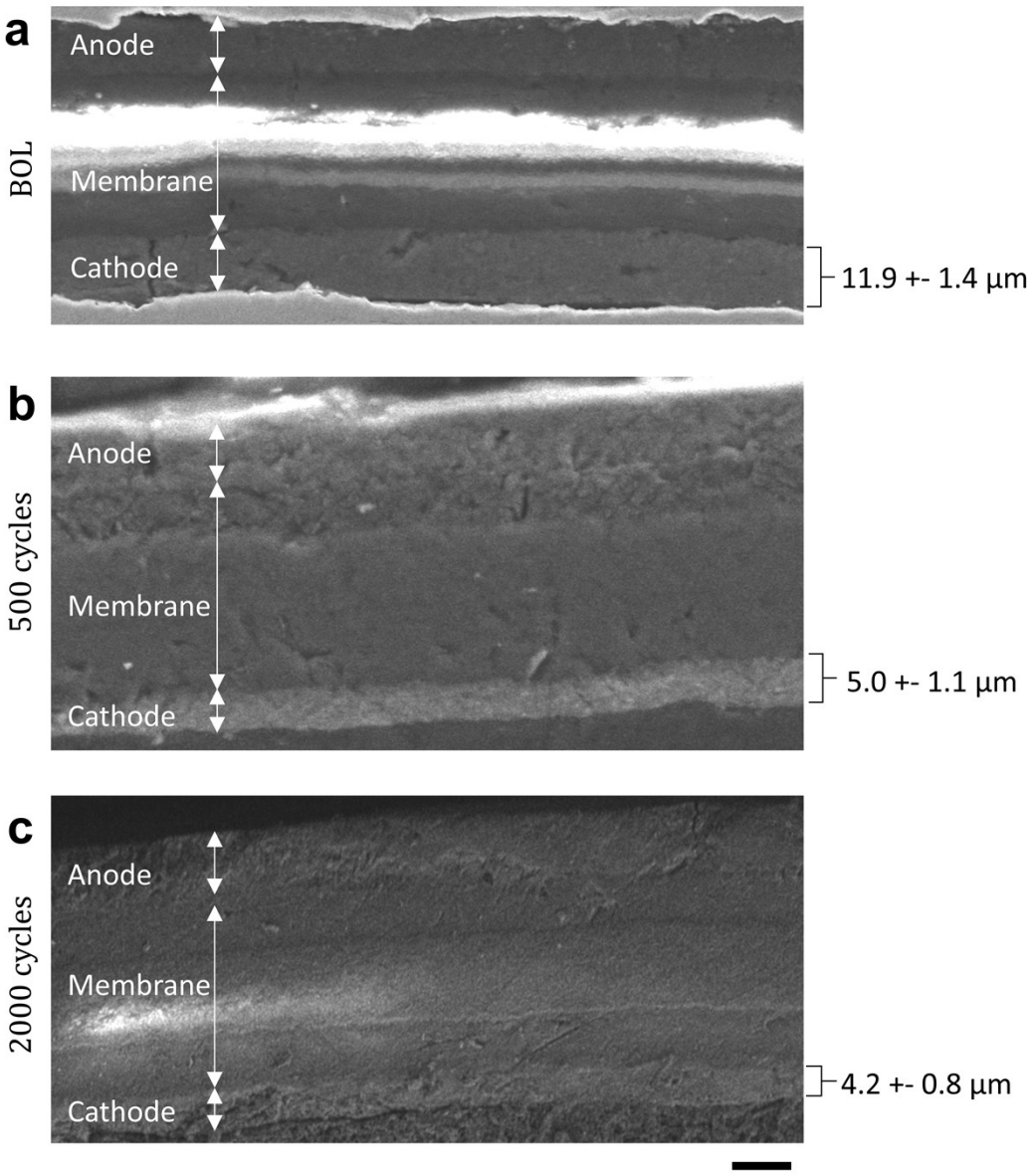

Figure S3| Reduction in thickness of cathode catalyst layer due to carbon corrosion. a, BOL. b, After 500 AST cycles. c, After 2000 AST cycles. The bright spots are due to charge accumulation in the membrane which is electronically non-conductive. Scale bar is 10 µm.

S5| Fitting AC impedance data with transmission line model:

To fit the electrical impedance spectroscopy data for a porous electrode, one requires a transmission line model rather than a Randles circuit. A transmission line can be thought to be a collection of a large number of Randles circuits consisting of infinitesimally small electrical circuit components like ion transport resistance, double layer capacitance, charge transfer resistance etc. A typical transmission line circuit looks like the following:

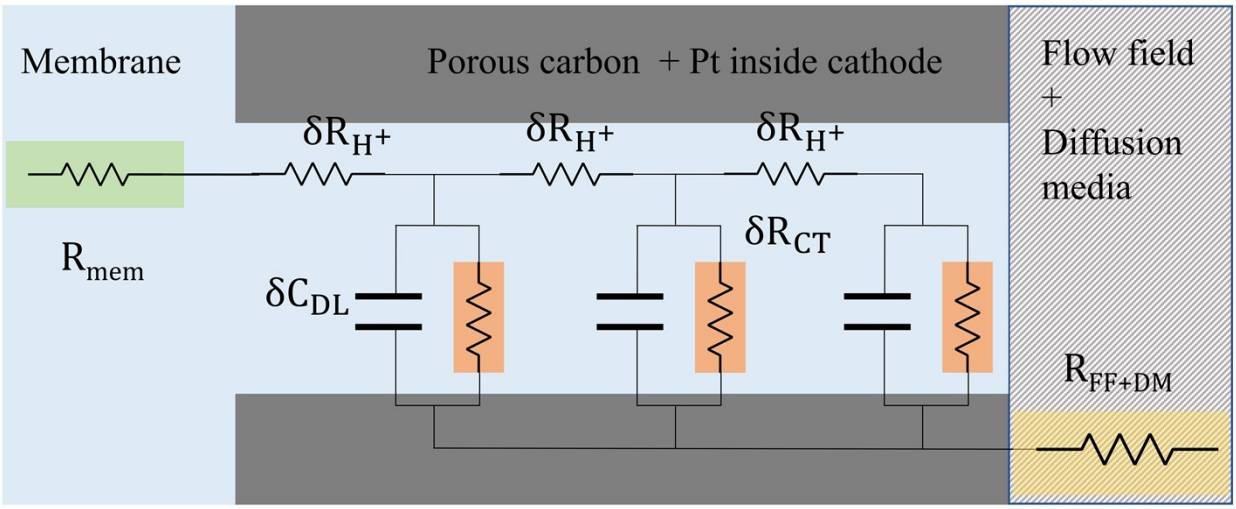

Figure S4| Schematic of a transmission line setup for a PEFC electrode.

Figure S5 shows three regions of interest for fitting EIS data of a porous cathode catalyst layer in PEFC- the membrane, cathode catalyst layer, diffusion media (DM) and the flow field (FF). R_{mem} is denoted as the bulk H^+ transport resistance through the membrane and R_{FF+DM} is the electronic resistance. The cathode catalyst layer also has some electronic resistance, but it is usually negligible compared to the H^+ transport resistance inside CCL. Inside CCL, $R_{Sheet} = N \times \delta R_{H^+}$ and $C_{Sheet} = N \times \delta C_{DL}$ with $N \to \infty$ where N is the number of circuit elements. R_{Sheet} and C_{Sheet} are the overall proton transport resistance and capacitance in the cathode catalyst layer. These are macroscopic quantities that can be related to experiments. The EIS was performed with H_2/N_2 at anode/cathode. In this configuration, $\delta R_{CT} \to \infty$. Hence, charging of the electrode is mostly capacitive. In practice, charge transfer resistances due to Faradaic reactions like ionomer adsorption, H oxidation (crossover H_2) can show some impact at low frequency limit. However, in the high frequency limit, the above-mentioned assumptions work pretty well. The net impedance formula is[3]:

$$Z = j\omega L + R_{Ohmic} + \sqrt{\frac{R_{Sheet}}{j\omega C_{Sheet}}} cothcoth\left(\sqrt{j\omega R_{Sheet} C_{Sheet}}\right) \quad \#(S8)$$

In Eqn. (S8), $j = \sqrt{-1}$, $\omega = 2\pi\nu$ is the angular speed, and L = inductance coming from the electrical wires. $R_{Ohmic} = R_{mem} + R_{FF+DM}$. EIS data are fit to this formula using Levenberg-Marquardt technique by implementing a modulus-weighted complex nonlinear least-squares fitting method for data fitting and error estimates. MEA II (up to 500 AST cycles) and III (2000 cycles) were used for EIS. Fitted results (Nyquist, phase, modulus, real and imaginary parts of Z) for MEA III are plotted in Figure S6:

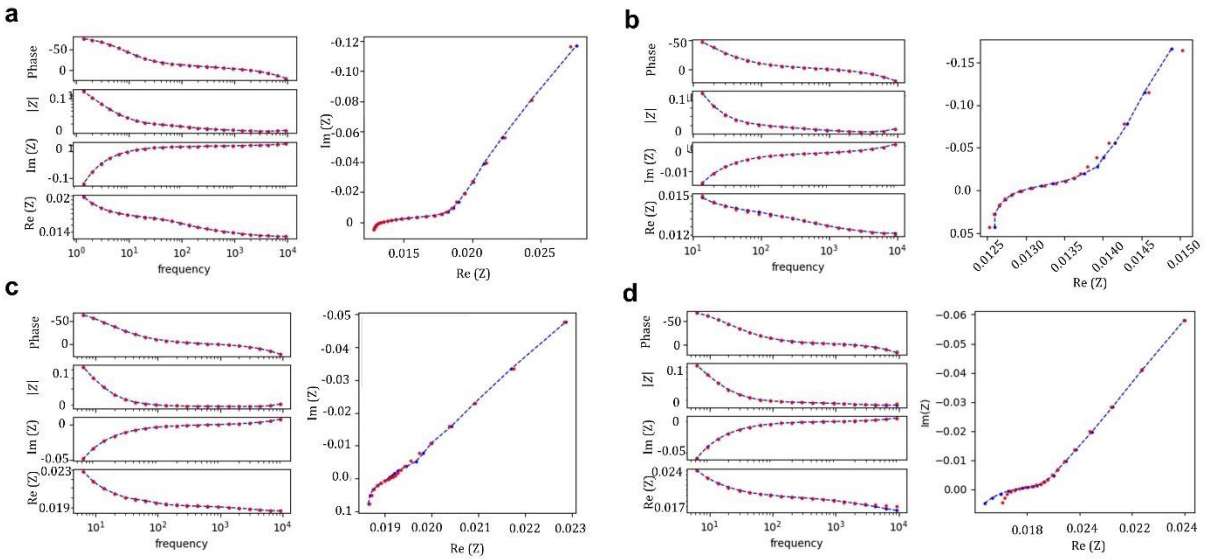

Figure S5| EIS fits are plotted for MEA III. a, BOL. b, After 100 AST cycles. c, After 500 AST cycles. d, After 2000 AST cycles. Deviations in the low frequency regime are due to the effect of Faradaic reactions that are not considered in Eqn. (S8). The deviation in the very high frequency end is due to the non-ideal inductance behavior. Blue dots are the experimental real and imaginary impedance vales, and the red dots are the corresponding fitted values.

The results for MEA II and III with standard errors (% values) are shown in Table S2 below.

Table S2| Ohmic resistance, sheet resistance, sheet capacitance and inductance fits for MEA II and III with standard error (in %)

Parameter	**R_{Ohmic} (mΩ-cm²)**		**R_{Sheet} (mΩ-cm²)**		**C_{Sheet} (mF-cm²)**		**L (µH-cm²)**	
Ageing state	**MEA III**	**MEA II**	**MEA III**	**MEA II**	**MEA III**	**MEA II**	**MEA III**	**MEA II**
BOL	61.5 1.05%	54.92 1.94%	84.34 3.7%	72.07 7.66%	222.8 0.61%	188.8 0.76%	2.77 6%	2.81 13.43%
100 AST cycles	61.28 0.67%	61.37 0.58%	20.11 9.99%	14.94 9.99%	181.2 3.74%	150 1.55%	2.42 5.88%	2.52 2.26%
500 AST cycles	92.15 0.35%	80.83 0.49%	10.64 9.92%	11.65 11%	125.66 1.53%	88.5 0.72%	4.25 1.18%	2.77 2.55%
2000 AST cycles	83.1 0.85%		29.02 12.5%		106.8 2.66%		2.71 9.97%	

In the above table, the inductance values for both MEAs remain the same. This should be the case as the inductance mostly comes from the electrical wires which do not change with carbon corrosion. It is also worth noting that the maximum errors are in estimating R_{Sheet}. With the values of R_{Sheet} and R_{Ohmic}, one can do the iR correction as:

$$\eta_{Ohmic} = i \times R_{eff} = i \times \left\{ R_{Ohmic} + \frac{R_{Sheet}}{3} \right\} \#(S9)$$

S6| FIB-SEM raw data:

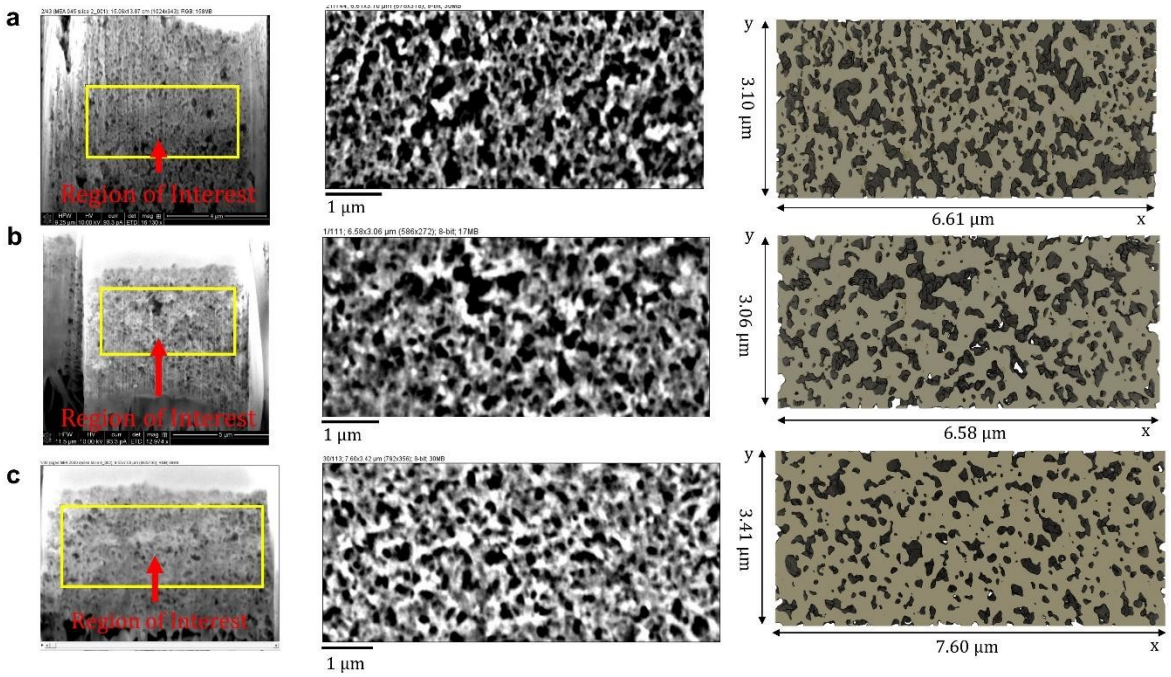

Figure S6| a, BOL b, 500 AST cycles and c, 2000 AST cycles. The first column shows the region of interest used for analysis from the raw FIB-SEM images. The region of interest excludes the areas that are either too close to the membrane or the platinum capping layers. The second column shows the raw grayscale images. The third column shows the segmented images. The color indicates solid phase (platinum, ionomer, and carbon).

A summary of the image acquisition and analysis has been provided in the experimental section of the main manuscript. The critical part about FIB-SEM analysis is finding the right contrast so that the pore space is properly visible. An SEM image fundamentally shows contrast between the solid and the void phase. When viewing an image slice, the next image slice may also affect the overall interpretation. For instance, if there is a layer of solid material just behind a pore, the pore may effectively look like a solid of slightly different contrast. In Figure S7 and S8, solid is denoted by white and the void is denoted by dark colors. At low contrast, pores were not sometimes visible because of the solid layer behind. The contrast was increased to account for this issue. If the contrast is too high, the solid substances with lower density will appear dark, and as a result, will be interpreted as void. So, at very low contrast, the pores are under-counted. At very high contrast, the pores are over-counted. For the final data analysis, an intermediate contrast setting was chosen to correctly estimate the pore volume.

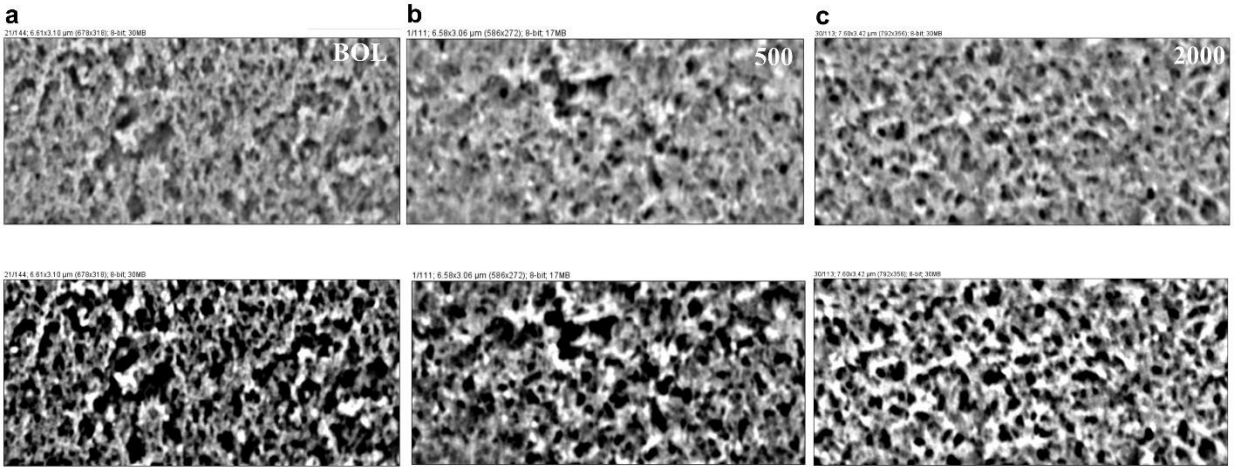

Figure S7| Role of contrast adjustment for a proper analysis of pore-space at a, BOL b, 500 AST cycles and c, 2000 AST cycles.

After proper segmentation, the images consist of correct pore and solid volumes. Local thickness procedure is performed on the pore-space to inscribe spherical kernels into each pore. Essentially, the largest possible sphere is being fit into the pore, and those voxels that belong to this sphere are ascribed to the diameter of the fit sphere. The pore-size distribution histogram is generated Then a bimodal log-normal distribution is fit to the discrete pore size distribution. Inside fuel cell catalyst layers, a bimodal pore size distribution is observed experimentally. The larger pores, known as the primary pores, are the void spaces between the carbon agglomerates. The smaller pores, called the secondary pores, are the void spaces inside each agglomerate. Uchida et al. were the first to suggest a bimodal pore size distribution inside catalyst layers from the mercury intrusion porosimetry data.[4] Log-normal distribution is usually fitted to the pore volume data of gas diffusion layers in fuel cell[5]. As a result, this was used in this study for the pore size distributions inside the catalyst layer as well. The following formula is used for fitting:

$$PDF\ (r) = \sum_{k\ =\ 1,2} f_{r,k} \left\{ \frac{1}{\sqrt{2\,\pi}\ r\ \sigma_k} exp\left[- \frac{\left(lnln\ r\ - lnln\ r_{o,k} \right)^2}{2\sigma_k^2} \right] \right\} \#(S9)$$

In Eqn. (S9), PDF stands for the probability density function. $f_{r,k}$ denotes the weight of the k'th distribution with the mean $r_{0,k}$ and the standard deviation σ_k. Clearly $f_{r,1} + f_{r,2} = 1$. The distribution mean is ($f_{r,1}$*$r_{0,1}$ + $f_{r,2}$*$r_{0,2}$). There are two mean diameter and standard deviation values reported- 1) quantities calculated from the segmented images itself, and 2) quantities calculated from the log-normal fits. In the main manuscript, the discussion is provided only with the earlier ones. The following data obtained for the pore size distribution at different stages of carbon corrosion is shown in Table S3

Table S3| Fitting parameters at BOL, after 500 AST cycles and after 2000 AST cycles.

Parameter	**Value at BOL**	**Value after 500 AST cycles**	**Value after 2000 AST cycles**
Mean diameter (nm)	50.6	72.1	55.7
Mode (nm)	22.1	48.0	40.9
Standard deviation (nm)	33.2	39.1	31.0

R^2 value	0.8	0.7	0.7
σ_1 (nm)	0.6	0.7	0.7
σ_2 (nm)	0.6	0.5	---
$r_{0,1}$ (nm)	55.6	61.1	56.8
$r_{0,2}$ (nm)	31.4	78.1	----
$f_{r,1}$ (nm)	0.8	0.6	1.0

S7| Linear sweep voltammetry (H_2 crossover current measurement):

H_2 crossover current is measured by linear sweep voltammetry (LSV). This current is added as a correction in the H_2/O_2 polarization curve to get a proper estimate of Tafel slope and exchange current density. Figure S9 and the table underneath show the LSV plots, and the currents used for crossover correction respectively. Data for MEA II and III were average up to 500 cycles, while the data for 2000 cycles is from MEA III.

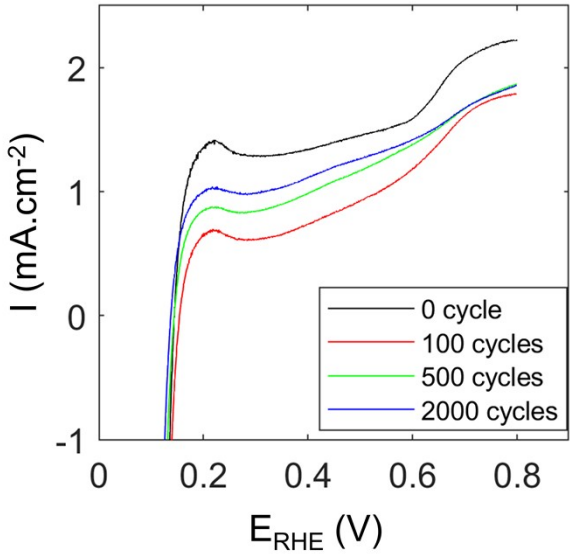

Figure S8| Linear sweep voltammetry data at BOL, after 100, 500 and 2000 AST cycles.

Table S4| Values of crossover current used for correction to generate Tafel plots.

AST stage	**$I_{crossover}$ (mA.cm^{-2})**	**$\Delta I_{crossover}$ (mA.cm^{-2})**
BOL	2.15	0.05
100 AST cycles	1.53	0.22
500 AST cycles	1.65	0.25
2000 AST cycles	1.6	

S8| Calculation of Tafel slope and concentration overpotential from H_2/O_2 polarization curve:

To calculate the concentration overpotential, first, the reversible potentials for H_2/O_2 and H_2/air case have to be calculated. Nernst equation for ORR can be written as:

$$E_{rev} = 1.23 \ - 0.0009(T - 298) + \frac{2.303RT}{4F} log\left[\left(\frac{P_{H_2}}{P_{H_2,ref}}\right)^2\left(\frac{P_{O_2}}{P_{O_2,ref}}\right)\right] \#(S10)$$

Where $P_{H2,ref}$ and $P_{O2,ref}$ are 1 atm each. These are the reference partial pressures at which the P independent quantities were calculated. (T-298) term is the temperature correction that comes from the temperature dependence of Gibbs free energy for ORR. For PEFC experiments, T = 353 K. The gas feeds (H_2 and O_2) are both 100% humidified. So, pressure of saturated water vapor has to be subtracted from the set backpressure to get the pressure of dry gas.

At T= 353 K, the pressure of saturated vapor pressure is = P_{sat} (80 C) = 47.343 kPa.

So, pressure of dry H_2 = P_{H2} = 151.988 – 47.343 kPa = 104.645 kPa.

For H_2/O_2 polarization curve, pressure of dry O_2 = P_{O2} = 151.988 – 47.343 kPa = 104.645 kPa.

Substituting all these values to Eqn. (S9), we get E_{rev} for H_2/O_2 polarization curves to be (vs RHE):

$$E_{rev}(O_2) = 1.23 - 0.0495 + 0.0175 \times log\left(\left[\frac{104.645}{101.325}\right]^3\right) = 1.181\ V$$

Next, the calculation of Tafel slope followed by the concentration overpotential.

Calculation of Tafel slope

First, the Butler-Volmer equation can be written in a way prescribed by Gasteiger et al[6]. The advantage of that way of writing the equation is that it is easy to relate with experimental parameters. It is also quite convenient for degradation studies, as one can isolate the quantities that can vary with degradation.

$$i = i_0\left(P_{O_2}, T\right) \times RF^{(k)} \times 10^{\frac{\eta_{kin}^{(k)}}{b}} \ \#(S11)$$

In Eqn. S11, i_0 is the exchange current density which depends on the catalyst nature, support structure, temperature and also on the partial pressure of O_2. The dependence on partial pressure of O_2 comes from the reaction order, which is approximately thought to be close to 0.5.[7] rf stands for the roughness factor which is the ratio between Pt ECSA and the geometric cell area. This is known for all AST stages (Figure

1d in the main manuscript). The current 'i' on the left-hand side has the unit of A.cm_{geo}^{-2} normalized to the cell geometric area. As rf is the ratio of Pt ECSA to the geometric active area ($cm_{Pt}^{2}.cm_{geo}^{-2}$), the unit of i_0 is $A.cm_{Pt}^{-2}$, i.e., it is normalized to the physical area of the Pt particles. η_{kin} refers to the kinetic overpotential. The superscript (k) denotes the AST stage (BOL, 100, 500, and 2000 cycles). The advantage of writing the Butler-Volmer equation like Eqn. S11 is that- the effect of degradation that is relevant in the kinetic region, i.e., loss of ECSA, and hence roughness can be isolated. The Eqn. S11 also easily shows that for the same current density i, the kinetic overpotential η_{kin} changes at different AST stages. As usual, 'b' refers to the Tafel slope.

Using the H_2/O_2 polarization curve in BOL, one can get BOL $\eta_{kin}(i)$ directly from the cell voltage data. Using the superscript 0 to represent the BOL data, we can write:

$$\eta_{kin}^{(0)}(i) = \eta^{(0)} - \eta_{Ohmic}^{(0)} = E_{rev} - E_{cell}^{(0)}(i) - i \times \left(R_{Ohmic}^{(0)} + \frac{1}{3} R_{Sheet}^{(0)} \right) \#(S12)$$

In Eqn. S12, $\eta^{(0)}$ is the experimentally measured overpotential, $E_{cell}^{(0)}(i)$ is the measured cell voltage at a particular current density. E_{rev} is 1.181 V. The most important assumption in Eqn. S11 is that at BOL, the concentration overpotential, i.e., $\eta_{conc}^{(0)} \approx 0$. This is certainly an approximation, but it is a common one used to calculate kinetic parameters in PEFCs. To make this approximation more justified, H_2/O_2 polarization curves are performed at high flow rates. With this definition of kinetic overpotential at BOL, one can rewrite the Eqn. S11 to get the Tafel slope and exchange current density i_0:

$$E_{cell}^{(0)} = E_{rev} - i \times \left(R_{Ohmic}^{(0)} + \frac{1}{3} R_{Sheet}^{(0)} \right) - b \times loglog\ i\ + bloglog\ i_0\ + bloglog\ RF^{(0)}\ \#(S13)$$

From, Eqn. S13, first, 'b' is estimated from the iR corrected curve (the first two terms on the right-hand side of the equation) and log(i) plot. From Figure 5a in the main manuscript, it is 71 mV/dec which is almost equal to the value found by Neyerlin et al.[7] for Pt/HSAC catalyst. Then, from the calculated Tafel slope, the exchange current density i_0 is calculated. For MEA II and III, we obtained values of $2.8 \times 10^{-8} A.cm_{Pt}^{-2}$ and $3.1 \times 10^{-8} A.cm_{Pt}^{-2}$. They are normalized to the Pt ECSA. Neyerlin et al., for 47% TKK catalyst, obtained $2.47 \pm 0.3 \times 10^{-8} A.cm_{Pt}^{-2}$[7]. So, the values reported in this study are only slightly higher than that obtained by Neyerlin et al., possibly due to different wt. % of catalyst and different fabrication methods.

Apparent increase in Tafel slope with carbon corrosion

If one assumes that the concentration potential $\eta_{conc} \approx 0$ for all stages of carbon corrosion, then one comes to an apparent fallacy- the Tafel slope increases with carbon corrosion. Basically, one assumes the validity of Eqn. S12 at all stages:

$$\eta_{conc}^{(k)} \approx 0 \Rightarrow \eta_{kin}^{(k)}(i) = \eta^{(k)} - \eta_{Ohmic}^{(k)} = E_{rev} - E_{cell}^{(k)}(i) - i \times \left(R_{Ohmic}^{(k)} + \frac{1}{3} R_{Sheet}^{(k)} \right) \#(S14)$$

If one calculates Tafel slope $b^{(k)}$, assuming the validity of Eqn. S12 for k= 0, 100, 500 and 2000, then the Tafel slope is found to change as shown in Table 5:

Table S5| Calculated Tafel slopes from polarization curves in oxygen at different stages of AST.

Ageing state	**Apparent Tafel slope**
BOL	71 (mV/dec)
100 AST cycles	76.8 (mV/dec)
500 AST cycles	87.4 (mV/dec)
2000 AST cycles	106.8 (mV/dec)

As discussed in the main manuscript, Tafel slope is related to the ORR activity on Pt. After carbon corrosion, it should not change as factors that affect the specific catalytic activity (normalized to the active area) like crystalline structure, defects etc. do not change after carbon corrosion. The only Pt property that changes after corrosion is its ECSA. So, there is no reason for the Tafel slope to change after carbon corrosion. As Tafel slope is calculated from iR corrected polarization curve, any change that might have occurred due to change in proton transport resistance can also be ruled out.

Calculation of concentration overpotential in H_2/O_2 setup assuming constant Tafel slope throughout AST

It is already well-known in the electrochemistry literature that mass transport limitation can cause wrong estimation of kinetic parameters. In the electrochemical corrosion industry specifically, this issue has been historically very important. Many innovative techniques have been developed to systematically remove the mass transport effects in the kinetic region. Often mass transport corrections are necessary to estimate kinetic parameters. In PEFCs, O_2 mass transport limitation is reduced by experimental setups- doing polarization curves in H_2/O_2 instead of H_2/air and high flow rate. This setup usually gives good results at the BOL. However, after carbon corrosion, O_2 MTR increases significantly. So, the same setup (flow rate, backpressure etc.) may not be sufficient to compensate for the increasing MTR after carbon corrosion. The increasing concentration overpotential with number of AST cycles can be explicitly calculated, with the logical assumption, that Tafel slope remains constant (BOL value of 71 mV/dec) in the following way:

At any AST stage, Eqn. S11 is valid. If one writes down the Eqn. S11, with the same current density at BOL and another AST stage ‘k’ (k = 100, 500, or 2000 cycles), one gets:

$$i = i_0\left(P_{O_2}, T\right) \times RF^{(k)} \times 10^{\frac{\eta_{kin}^{(k)}}{b}} = i_0\left(P_{O_2}, T\right) \times RF^{(0)} \times 10^{\frac{\eta_{kin}^{(0)}}{b}} \#(S15)$$

Eqn. S15 is convenient to use as polarization curves (both H_2/O_2 and H_2/air) are performed at known current densities which are kept the same. $\eta_{kin}^{(0)}$ can be obtained from the H_2/O_2 polarization curve data using Eqn. S12. Thus, knowing $\eta_{kin}^{(0)}$, one can predict $\eta_{kin}^{(k)}$ where k= 100, 500 or 2000 cycles from:

$$\eta_{kin}^{(k)} = \eta_{kin}^{(0)} + b \times loglog\left\{\frac{RF^{(0)}}{RF^{(k)}}\right\} \#(S16)$$

In Eqn. S16, rf values are known at all AST stages (Figure 1d main manuscript). Tafel slope 'b' is set constant at the BOL value of 71 mV.dec^{-1}. The exchange current density does not change as it is a catalyst specific parameter. In addition, ohmic overpotential can be easily estimated as:

$$\eta_{Ohmic}^{(k)} = i \times \left(R_{Ohmic}^{(k)} + \frac{1}{3}R_{Sheet}^{(k)}\right) \#(S17)$$

The data for R_{Ohmic} and R_{Sheet} are known for all stages from EIS measurements, as shown in Figure 3b and 3c in the main manuscript and Table S2 in section S5. So, the remaining overpotential, i.e., concentration overpotential coming from O_2 mass transport limitation can be found from:

$$\eta_{conc}^{(k)} = \eta^{(k)} - \eta_{kin}^{(k)} - \eta_{Ohmic}^{(k)} = \left\{E_{cell}^{(0)}(i) - E_{cell}^{(k)}(i)\right\} - b \times loglog\left\{\frac{RF^{(0)}}{RF^{(k)}}\right\} \times \left(\left[R_{Ohmic}^{(k)} - R_{Ohmic}^{(0)}\right] + \frac{1}{3}\left[R_{Sheet}^{(k)} - R_{Sheet}^{(0)}\right]\right) \#(S18)$$

In Eqn. S18, we have combined the Eqns. S12, S16 and S17. Note that Eqn. S18 is written in such a way that it only contains those parameters that are directly found from the experiments. Applying Eqn. S16 to the H_2/O_2 polarization curve with the known parameters produces Figure 5b in the main manuscript.

S9| Calculation of concentration overpotential from H_2/air polarization curve:

To calculate the concentration overpotentials, firstly the reversible potential for H_2/air setup is needed. It can be calculated from Eqn. S10. The only difference with the previous calculation for H_2/O_2 setup is in the O_2 partial pressure. In air, O_2 consists approximately $1/5^{th}$ of the number density. Saturated vapor pressure, again, is 47.343 kPa at 80° C. The set backpressure at anode and cathode is 1.5 atm or 151.988 kPa.

So, for H_2/air polarization curve, pressure of dry $O_2 = P_{O2} = 1/5 * (151.988 - 47.343) = 20.929$ kPa.

Similarly, we get the H_2/air polarization curve (vs RHE) from Eqn. S9:

$$E_{rev}(air) = 1.23 - 0.0495 + 0.0175 \times log\left(\left[\frac{104.645}{101.325}\right]^2 \times \left[\frac{20.929}{101.325}\right]\right) = 1.1685\ V$$

Tafel slope and the exchange current density are already determined in section S8 as 71 $mV.dec^{-1}$ and $2.95 \times 10^{-8}\ A.cm_{Pt}^{-2}$ (average of MEA II and III). So, one can estimate the kinetic overpotential $\eta_{kin}^{(k)}$ at any stage of AST using Eqn. S11. $\eta_{Ohmic}^{(k)}$ can also be calculated from the known values of R_{Ohmic} and R_{Sheet} at different AST stages. Experimentally, one can measure the overpotential $\eta^{(k)}(i)$ at any current density. From these quantities, one can estimate the concentration overpotential at any stage of AST:

$$\eta_{conc}^{(k)}(i) = \eta^{(k)}(i) - \eta_{kin}^{(k)}(i) - \eta_{Ohmic}^{(k)}(i) = E_{rev} - E_{cell}^{(k)}(i) - b \times loglog\left[\frac{i}{i_0 \times RF^{(k)}}\right] - i \times \left(R_{Ohmic}^{(k)} + \frac{1}{3}R_{Sheet}^{(k)}\right) \#(S19)$$

Thus, from Eqn. S19, concentration overpotential at BOL can be explicitly calculated and need not be approximated as 0. Note that in H_2/O_2 setup, the approximation of $\eta_{conc}^{(0)}(i) = 0$ is necessary, otherwise the kinetic parameters cannot be calculated as no exact analytical formula for concentration overpotential that can be applied to PEFC exists in literature.

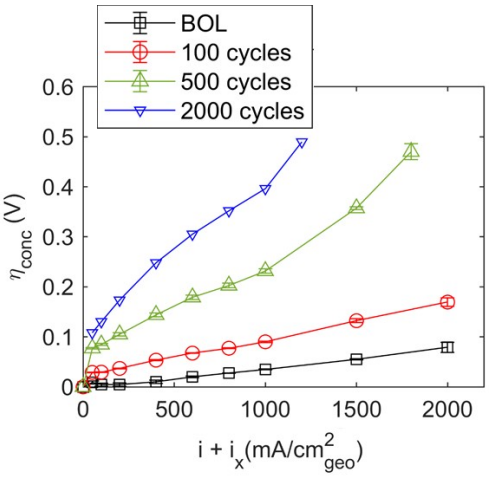

Figure S9| Concentration overpotential (in air) as a function of current density at different stages of carbon corrosion. I_x is the correction due to hydrogen crossover current.